Structural Engineering and Mechanics, *Vol. 71, No. 4 (2019) 363-375*
DOI: https://doi.org/10.12989/sem.2019.71.4.363

Nonlinear responses of energy storage pile foundations with fiber reinforced concrete

Saule Tulebekova[a], Dichuan Zhang*, Deuckhang Lee[b], Jong R. Kim[c], Temirlan Barissov[d] and Viktoriya Tsoy[d]

Department of Civil and Environmental Engineering, Nazarbayev University, 53 Kabanbay Batyr Ave, Nur-Sultan, Republic of Kazakhstan

(Received March 15, 2019, Revised April 1, 2019, Accepted April 5, 2019)

Abstract. A renewable energy storage pile foundation system is being developed through a multi-disciplinary research project. This system intends to use reinforced concrete pile foundations configured with hollowed sections to store renewable energy generated from solar panels attached to building structures in the form of compressed air. However previous research indicates that the compressed air will generate considerable high circumferential tensile stresses in the concrete pile, which requires unrealistic high hoop reinforcement ratio to avoid leakage of the compressed air. One possible solution is to utilize fiber reinforced concrete instead of placing the hoop reinforcement to resist the tensile stress. This paper investigates nonlinear structural responses and post-cracking behavior of the fiber reinforced concrete pile subjected to high air pressure through nonlinear finite element simulations. Concrete damage plasticity models were used in the simulation. Several parameters were considered in the study including concrete grade, fiber content, and thickness of the pile section. The air pressures which the pile can resist at different crack depths along the pile section were identified. Design recommendations were provided for the energy storage pile foundation using the fiber reinforced concrete.

Keywords: fiber reinforced concrete, pile foundation, nonlinear structural responses, compressed air, renewable energy storage

1. Introduction

Renewable energy, widely used for buildings with solar panels or wind mills attached to (Hayter and Kandt 2011), has a nature of intermittency. This intermittent nature, due to climate and day-and-night diurnal cycles, does not allow for an uninterrupted energy supply (Rugolo and Aziz 2012). One of solutions is to store extra renewable energy when it is available and release it for later use. One of prominent technologies for energy storage is compressed air energy storage (CAES) (Zhang *et al*. 2012, Kim *et al.* 2017). Utilizing CAES, a renewable energy storage pile foundation system is being developed through a multi-disciplinary research project (Sabirova *et al.* 2016, Tulebekova *et al.* 2017). This system intends to use reinforced concrete pile foundations configured with hollowed sections to store renewable energy generated from solar panels attached to buildings in the form of compressed air.

*Corresponding author, Assistant Professor
E-mail: dichuan.zhang@nu.edu.kz
[a] Research Assistant
E-mail: stulebekova@nu.edu.kz
[b] Assistant Professor
E-mail: deuckhang.lee@nu.edu.kz
[c] Professor
E-mail: jong.kim@nu.edu.kz
[d] Undergraduate student

An analytical study using three-dimensional (3D) finite element models was conducted for regular reinforced concrete pile foundations (Zhang *et al.* 2018). The results of the finite element analyses showed that the pressure from the compressed air is significant, which generates considerably high tensile circumferential stresses in the pile section. These tensile stresses cause cracking of the concrete, which can lead to the leakage of air and damages of the pile. Hoop reinforcement placed in the pile has potential to resist these tensile stresses. However, from analytical results, the needed hoop reinforcement for preventing full section cracking is quite high (ranged from 3 to 6%) due to the strain compatibility between steel and concrete. This high hoop reinforcement ratio can result in difficulties in the construction of the pile foundation.

Alternative solutions are available for the energy storage pile foundation to resist the high tensile stress including: (1) developing high performance concrete with a tensile strength safely higher than the demand from the compressed air (Bektimirova *et al.* 2017, Bektimirova *et al.* 2018); (2) utilizing steel pipes as the pile foundations (Ko *et al.* 2018); (3) using steel tubes filled with concrete for the pile foundations (Agibayeva *et al.* 2018); (4) replacing the regular reinforced concrete with the fiber reinforced concrete with semi-ductile post-cracking behaviors.

This paper investigates the last option of using the fiber reinforced concrete for the energy storage pile foundation through nonlinear finite element simulations. Several parameters were considered in this paper including concrete grade, fiber content and thickness of the pile section.

http://www.techno-press.com/journals/sem&subpage=7 ISSN: 1225-4568 (Print), 1598-6217 (Online)

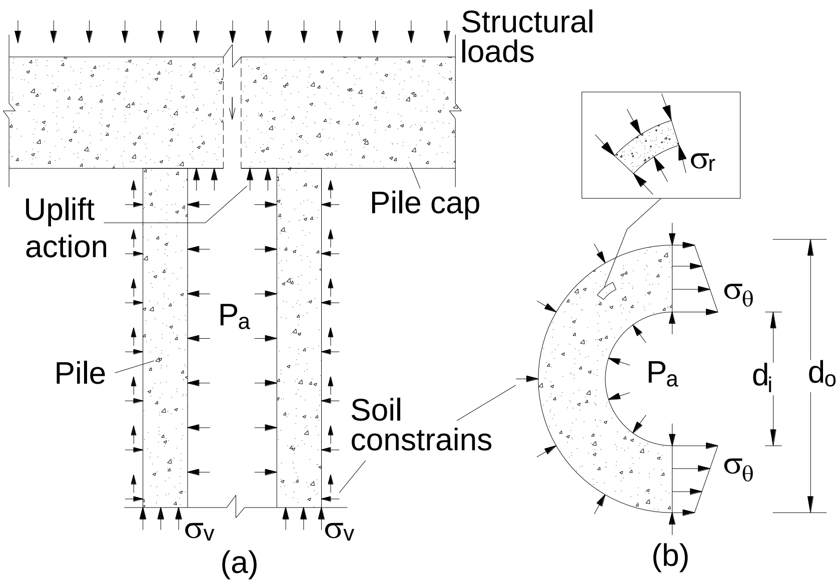

Fig. 1 Stresses in the pile foundation: (a) vertical stresses; (b) circumferential and radius stresses

Nonlinear static analyses were conducted using two-dimensional (2D) plane strain models with concrete damage plasticity. The 2D model was subjected to an increasing pressure up to the crack penetrating through the entire pile section, after which the leakage of air is expected to occur and the energy storage function of the pile foundation will lose. The post-cracking behavior of the fiber reinforced concrete was examined. The air pressures which the pile can resist at different crack depths along the pile section were identified. By comparing analytical results with pressure demands for typical buildings, design recommendations were provided for the energy storage foundation using the fiber reinforced concrete.

2. Background

2.1 Stresses in pile foundations

The proposed energy storage pile foundation is typically subjected to loads from the superstructure, constrains from surrounding soils and applied pressure (P_a) from the compressed air as shown in Fig.1. Under these combined actions, the pile section will develop three stress components: vertical stress (σ_V), circumferential stress (σ_θ), and radial stress (σ_r). From the analytical results in Zhang *et al*. (2018), the following findings were observed: (1) the air pressure generates significant tensile circumferential and compressive radial stresses with a non-uniform distribution along the radius direction of the pile section (see Fig. 1b). The non-uniform distribution of the stress provides an opportunity to use the hoop reinforcement or the fiber reinforced concrete to limit the crack depth along the pile section; (2) the soil constrains generate trivial circumferential and radial stresses comparing to those from the compressed air. Moreover, the circumferential stress from the soil constrains is in compression, which will reduce the tensile stress from the compressed air; (3) the vertical stress from the structural loads is insignificant and reduced by the uplifting action from the compressed air (See Fig. 1a).

Since the effects of the structural loads and the soil constrains are limited and provide favorable conditions comparing with the compressed air, this paper focuses on the nonlinear behavior of the concrete pile section under the air pressure using the 2D plane strain model without considering the structural loads and the soil constrains. Thus, the results presented in this paper are also applicable to general concrete cylinder containers subjected to high inside pressures.

2.2 Fiber reinforced concrete

In cases where the structures undergo significant complicated loading, such as in large slabs, shear walls and energy storage pile foundations discussed in this paper, reinforcement ratio for regular concrete is unconventionally high. Due to this phenomenon, several issues are encountered such as rebar crowding and low workability of concrete (Lee *et al.* 2016). Fiber reinforced concrete has potential to overcome this issue with its considerable high tensile strength and semi-ductile post-cracking behavior. The increase of tensile strength and ductility is originated from high strength fibers (typically in hooked shapes) such as steel fiber (Kwak *et al.* 2002), polyethylene fiber (Yu *et al.* 2017), polyvinyl fiber (Zhu *et al.* 2018), and glass fiber (Yoo and Banthia 2015). The effectiveness of fibers on increasing the tensile strength and ductility is largely dependent on the fiber content as well as the concrete grade (strength). The higher strength of concrete, the more bonding can be formed between the fiber and concrete. Thus, in turn, higher tensile strength and ductility can be obtained compared to the regular concrete (Kwan and Chu 2018). Therefore, this paper used the concrete grade and the fiber content as study parameters for the fiber reinforced concrete.

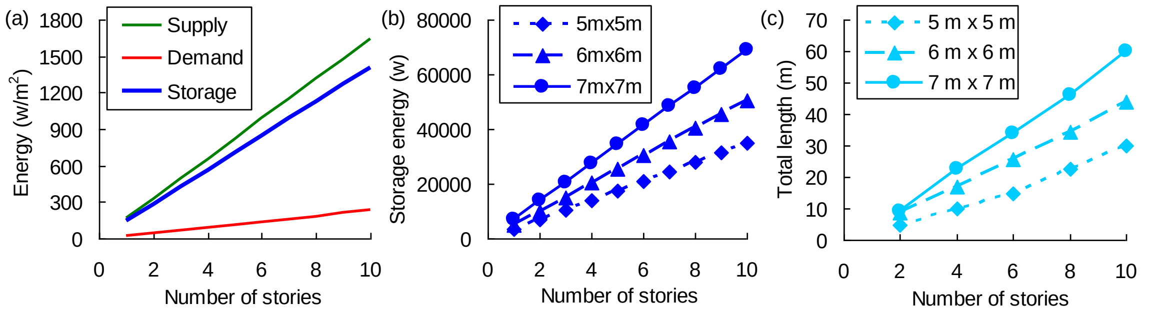

Fig. 2 Storage energy and pile design: a) energy for typical residential buildings; (b) available energy for storage for each column; (c) required total length of the pile for each column

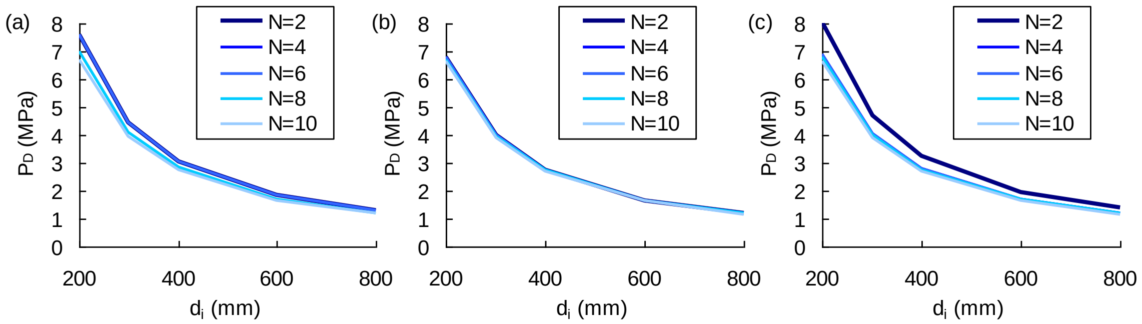

Fig. 3 Pressure demand: a) 5x5 m column space; (b) 6x6 m column space; (c) 7x7 m column space

2.3 Pressure demand on piles

The pressure demand (P_D) on the pile can be calculated using thermodynamic cycles of CAES with available energy for storage ($\dot{w}_{in}$) and available volumes for storage (V_s) by solving an implicit equation (Eqn.1). The more available energy and the less available volume for storage are, the higher pressure demand is. The detailed derivation of Eqn.1 can be found in Zhang *et al*. (2018).

$$\frac{P_D V_s}{RT_1} = \frac{\dot{w}_{in} t_{in} \eta_1}{3.5R[C^{7/5}(P_D/T_1)^{2/5} - T_1]} + \rho_i V_s / \mu \quad (1)$$

where, R is the universal gas constant; T_1 is the ambient air temperature; C is a constant taken as 10.89; t_{in} is the time for compressing air; ρ_i and μ are the initial density and molar mass of the air, taken 1.2 kg/m3 and 0.029 kg/mol respectively; η_1 is the efficiency for compressing the air.

The available energy for storage can be determined as differences between energy supplies from solar panels and energy demand from the end-users. Figure 2a shows the energy supply, the energy demand and the available energy for storage per unit floor area for typical residential buildings ranged from 2 to 10 stories. The energy supply was obtained from experimental data of solar panels and the energy demand was estimated from typical residential buildings in Astana, Kazakhstan, as discussed in Zhang *et al*. (2018). Figure 2b shows the available energy for storage for each column with different column spaces and numbers of stories. As seen, as the column space and the number of stories increase, the available energy for storage increases.

The available volume for storage for each column is dependent on the length of pile, number of piles and the inner diameter (d_i) of the pile. The length of pile and number of piles for each column were determined from the geotechnical design by assuming the outer diameter (d_o) of pile as 1 m as discussed in Zhang *et al*. (2018). The maximum inner diameter of the pile was determined as 800mm for safely carrying the vertical structural loads as discussed in Zhang *et al*. (2018). Figure 2c shows total pile length (length of each pile multiplied by number of piles) for each column, which increases as the column space and number of stories increases due to the increase of the vertical structural load.

Figure 3 shows the pressure demand (P_D) vs. different column spaces, numbers of stories and inner diameters of the pile section. As seen in Fig. 3, the pressure demand shows similar values for different column spaces and numbers of stories because both the available energy and the volume for storage increases as the increase of the column space and the number of stories. On the other hand, the inner diameter (d_i) of the pile only affects the available volume of storage and plays an important role on the magnitude of the pressure demand. Thus, the inner diameter of the pile was used as one of study parameters in this paper.

3. Parametric study

3.1 Concrete properties

This paper adopted four different grades of concrete (C30, C60, C150 and C250) and four different steel fiber contents (1%, 1.5%, 2% and 3%) as study parameters for the fiber reinforced concrete. The C30 and C60 concrete

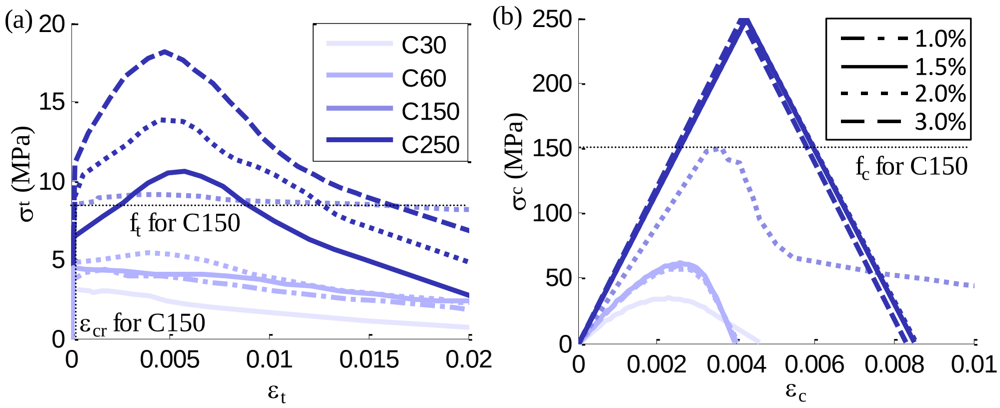

Fig. 4 Stress-strain curves of the fiber reinforced concrete: (a) tension; (b) compression

Table 1 Properties of fiber reinforced concrete from tests

Grade of concrete	Fiber content (%)	Compressive strength (f_c) (MPa)	Tensile strength (f_t) (MPa)	Young's modulus (E) (MPa)	Cracking strain ($\varepsilon_{cr} = f_t / E$)	References
C30	1.5	34.5	3.11	24566	0.000127	Lee *et al.* 2016
C60	1.0	57.4	4.02	31781	0.000126	Kwan and Chu 2018
	1.5	58.9	4.43	32185	0.000138	
	2.0	61.3	4.8	32833	0.000146	
C150	2.0	150	8.5	45550	0.000187	Hassan *et al.* 2012
C250	1.5	250	6.4	58500	0.000109	Wille *et al.* 2014
	2.0	250	9.0	60290	0.000149	
	3.0	250	11.1	58670	0.000189	

refer as fiber reinforced concrete (Lee *et al.* 2016) (Kwan and Chu 2018) while the C150 and C250 concrete refer as ultra-high-performance concrete (Hassan *et al.* 2012) (Wille *et al.* 2014). Table 1 shows the properties of the fiber reinforced concrete obtained from tests.

To investigate the post-cracking behavior of the concrete pile foundation, a key step is to obtain tensile stress-strain relations of the fiber reinforced concrete from direct tension tests. This paper utilized the direct tension test results for the fiber reinforced concrete listed in Table 1 from four research groups (Lee *et al.* 2016) (Kwan and Chu 2018) (Hassan *et al.* 2012) (Wille *et al.* 2014). The tensile and compression stress-strain relations are shown in Fig.4, where double-legend approach is used: different colors representing different concrete grades and different line types representing different fiber contents. This approach will be used for all the figures in this paper when the concrete grade and fiber content are presented together. As an example, the f_t, ε_{cr}, and f_c listed in Table 1 are indicated as trend lines for the C150 concrete, where f_t and ε_{cr} refer to starting point of the nonlinear response in Fig. 4a and f_c refers to the peak strength point in Fig. 4b.

Figure 4a shows the uniaxial tensile stress-strain curves from the direct tension test results. As the concrete grade and the fiber content increase, the tensile strength increases and the rate of strength reduction after cracking becomes slower. Hardening behavior after cracking is even observed in the C250 concrete.

Figure 4b shows the uniaxial compression stress-strain curves. Experimental stress-strain data were available only for the C150 concrete provided in Hassan *et al.* (2012). The empirical constitution model provided in the *fib* (2008) was used for developing the compression stress-strain curves for other grades except for the C250 concrete using the f_c and E values in Table 1. Since concrete with extremely high strength exhibits brittle behavior in compression, the stress-strain curves for the C250 concrete were assumed to be bi-linear as seen in Fig. 4b.

The stress-strain curves shown in Fig.4 and the concrete properties listed in Table 1 were used to develop the input parameters for the concrete damage plasticity model which will be discussed in the Section 3.3.

3.2 Design of the pile foundation

The design of pile foundation followed the industry practice and the design procedure as discussed in Section 2.3. This paper used five different inner diameters of the pile section (d_i= 200 mm, 300 mm, 400 mm, 600 mm and 800 mm) as one of study parameters since the inner diameter plays an important role on the pressure demand (P_D) as mentioned in Section 2.3.

3.3 Analytical model

The analytical model of the pile foundation was built using the general-purpose finite element software ABAQUS as shown in Fig. 5. A 2D plane strain model was constructed to represent a quarter of a whole pile section because of symmetry. A relatively fine mesh (~10 mm by 10 mm) was applied for a precise representation of the stress and strain distribution along the radius direction of the pile. Symmetry boundary conditions were applied as shown in Fig.5. The pressure (P_a) from the compressed air was applied at the inner surface with increasing amplitudes till the crack penetrated through the entire cross-section, after which the leakage of air is expected to occur, similar as the pushover analysis used in structural seismic studies (Wan *et al.* 2012, 2015, Zhang *et al.* 2016). The structural loads and soil constrains were ignored in this

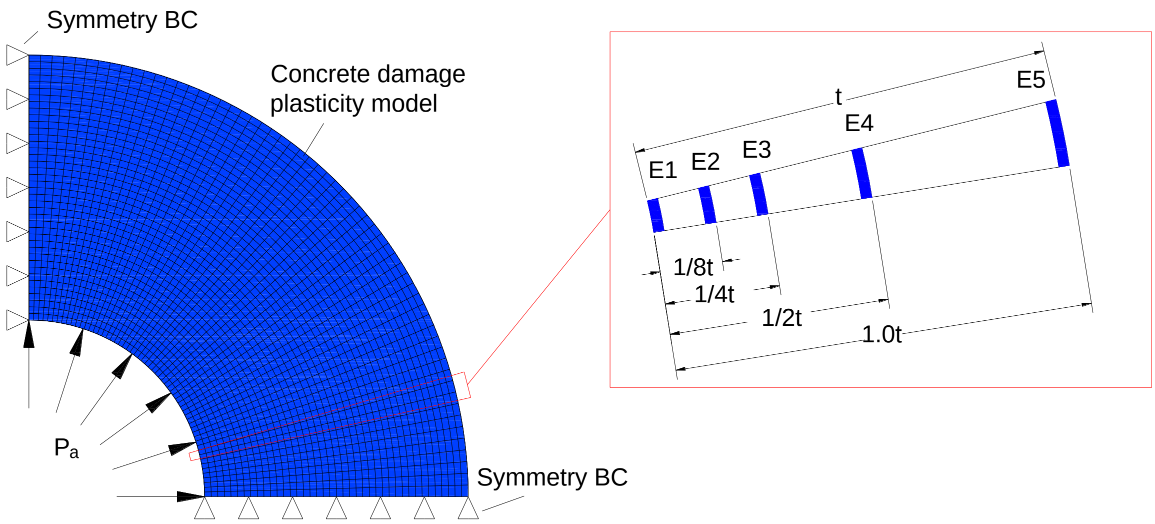

Fig. 5 2D plane strain model for the pile section

Table 2 Plasticity parameters for concrete damaged plasticity model (Hafezolghorani *et al.* 2017)

Dilation angle, ϕ	Eccentricity, ε	f_{b0}/f_{c0}	K	Viscosity, μ_v
31 degree	0.1	1.16	0.67	0.0001

model as discussed in Section 2.1. The insert in Fig. 5 shows a zoom-in of a strip of elements along the radius direction with five of them (E1 to E5) marked out which will be used for presenting analytical results in Section 4. The variable t in Fig. 3 stands for the thickness of the section and can be calculated as $t = (d_o\text{-}d_i)/2$.

The material model of the fiber reinforced concrete are the concrete damage plasticity model (ABAQUS 2010). The concrete damage plasticity model uses the concepts of isotropic damage with tensile cracking and compressive crushing failure mechanisms. The input parameters include uniaxial tension stiffening and damage model; uniaxial compression hardening and damage model; and multi-axial plasticity model. The input parameters for uniaxial tension and compression models were derived from the stress-strain curves in Fig. 4 and the concrete properties listed in Table 1 following the procedure used in Wahalathantri *et al.* (2011). The multi-axial plasticity model follows the Drucker-Prager plasticity (Drucker and Prager 1952). The plasticity parameters for the flow potential function and the shape of the yield function were obtained from the guidelines proposed by Hafezolghorani *et al.* (2017). Table 2 shows the summary of the input plasticity variables, where ϕ is dilation angle (in degrees), ε is eccentricity, f_{b0}/f_{c0} is the ratio of biaxial compressive stress to uniaxial compressive stress, K is the ratio of the second stress invariant on the tensile meridian to that on the compressive meridian, μ_v is the viscosity parameter.

A damage parameter (SDEG) in the concrete damage plasticity model was used to represent stiffness degradation as the increase of the plastic response. The damage parameter varies between 0 and 0.99, where the zero representing non-damage state while the 0.99 representing fully damage state (1.0 was not used to avoid non-convergence during the simulation). The non-damage state is defined as states where both tension and compression remain elastic. The fully damage state is defined as a state where tension or compression reaches the zero strength.

4. Analytical results

4.1 General structural response

The general structural response of the pile foundation is discussed in this section using the C30 and fiber content of 1.5% with d_i=200mm as an example. The stress and strain responses, post-carking behaviors, stress redistributions and damages of the concrete are examined and presented.

Figure 6 shows the contour of the circumferential strain (ε_θ) at two different applied pressures (P_a). The grayed area in Fig. 6 represents that the ε_θ is larger than the cracking strain (ε_{cr}) defined in Table 1. Thus, the depth of the grayed area can be used to indicate crack depth (d_{cr}) along the radius direction (r) as annotated in Fig.6. Figure 6a shows the crack penetrating halfway through the pile section, whereas Fig.6b shows the crack penetrating nearly to the entire pile section. As noticed in Fig. 6, the distribution of the ε_θ along the circumferential direction (θ) is uniform. Therefore, the rest of paper will only present results for one strip of the elements along r direction at θ=0.

Figure 7 shows the circumferential stress (σ_θ) and strain (ε_θ) vs. applied pressure (P_a) for the five representing element along the r direction (refer to Fig. 5). The tensile strength (f_t) and cracking strain (ε_{cr}) are indicated as horizontal trend lines in Fig.7a and 7b respectively.

As seen in Fig. 7a, the circumferential stress increases as the increase of the applied pressure till a point where the concrete cracks and exhibits post-cracking strength degrading behavior. This point is corresponding to $\varepsilon_\theta = \varepsilon_{cr}$ and can be defined as a cracking point as shown in Fig. 7b. The element closest to the inner surface (E1) first reaches the cracking point, and then the σ_θ of E1 starts to decrease. Due to stress redistribution, other elements along the r

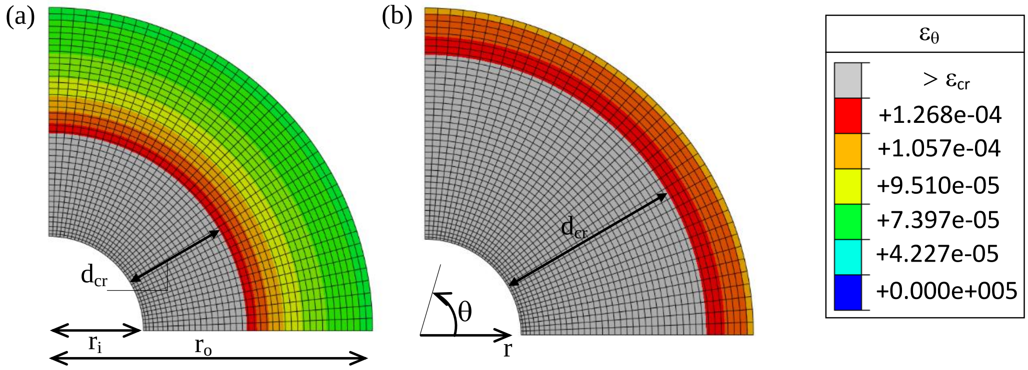

Fig. 6 Circumferential strain contour at: (a) P_a=9.1 MPa; (b) P_a=10 MPa

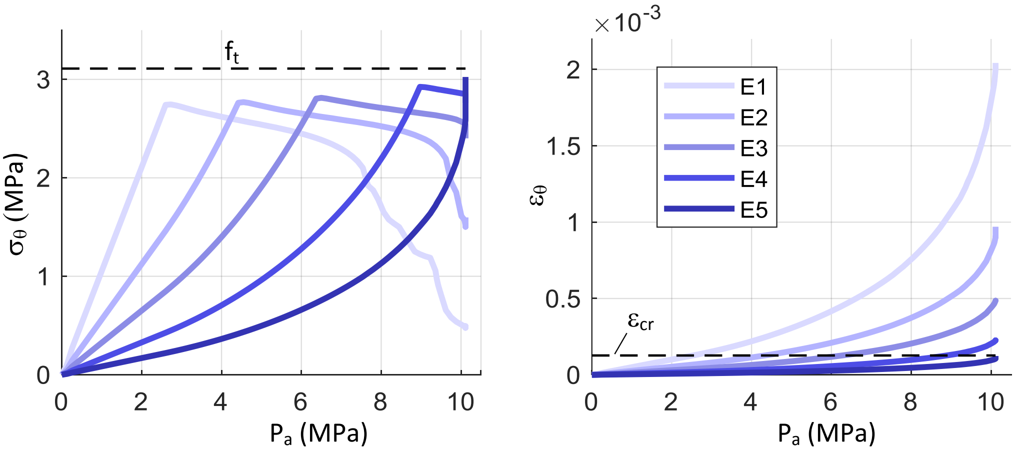

Fig. 7 Circumferential response vs. applied pressure for the five representing elements: (a) stress; (b) strain

direction gradually reach the cracking point in sequence as P_a increases. At the end of loading, the ε_θ in all the elements exceeds the ε_{cr} (see Fig. 7b), which indicating the fully penetration of the crack through the pile section. Severer strength degradation is observed for the elements closer to the inner surface. As noticed in Fig.7a, the circumferential stress in all the elements starts to decrease before reaching the tensile strength. This behavior is caused by combined effects from tension in the θ direction and compression in the r direction, which will be discussed further in Fig. 8.

Figure 8 shows the stress-strain responses of the five representing elements in the circumferential direction (σ_θ vs. ε_θ) and the radius direction (σ_r vs. ε_r). The uniaxial backbone responses from Fig.4a for tension and Fig.4b for compression are indicated as dashed lines in Fig.8a and 8b respectively. As seen in Fig. 8a, the combined tension (σ_θ) and compression (σ_r) stress causes reduction of tensile strength and a more rapid strength degradation after cracking in the circumferential direction comparing to the uniaxial response. On the other hand, in the radius direction as shown in Fig.8b, significant compression strength and stiffness reduction is observed because the concrete was loaded against its tensile strength limit in the circumferential direction. The element closer to the inner surface shows higher strength reduction in both tension and compression in consistent with the findings in Fig.7a.

Figure 9 shows the circumferential stress and strain distribution along the radius direction (r) under different applied pressure (P_a). The tensile strength (f_t) and cracking strain (ε_{cr}) are indicated as horizontal trend lines in Fig.9a and 9b respectively. As seen in Fig. 9a, when the P_a is low (2.5 MPa), the pile section remains elastic. The σ_θ reaches highest value at the inner surface and nonlinearly reduces as the increase of r, which is consistent with the results in Zhang *et al.* (2018). As the P_a increases, the pile section starts to exhibit strength degradation behavior from the inner surface gradually penetrating into the outer surface. The strength degradation causes stress redistribution along the radius direction. Eventually it reaches a state (P_a=10.1 MPa) where outer surface has the highest stress and gradually reduces as moving to the inner surface. This distribution is directly opposite to the one observed in the elastic state. On the other hand, as shown in Fig. 9b, the ε_θ remains the similar distribution along the r direction. The horizontal coordinate at the intersection between ε_θ and ε_{cr} for different curves in Fig. 9b represents the crack depth (d_{cr}) at different P_a.

Figure 10 shows the crack depth (d_{cr}) with the increase of the applied pressure (P_a). The absolute values are shown in Fig.10a. The normalized values are shown in Fig.10b, where the d_{cr} is normalized by the thickness (t) of pile section and the P_a is normalized by the tensile strength (f_t). The crack penetration increases with the increase of P_a. The penetration speed initially is slow and becomes faster as the P_a increases. When d_{cr} is large than 200mm (50% penetration), a small amount increase of the P_a leads to a

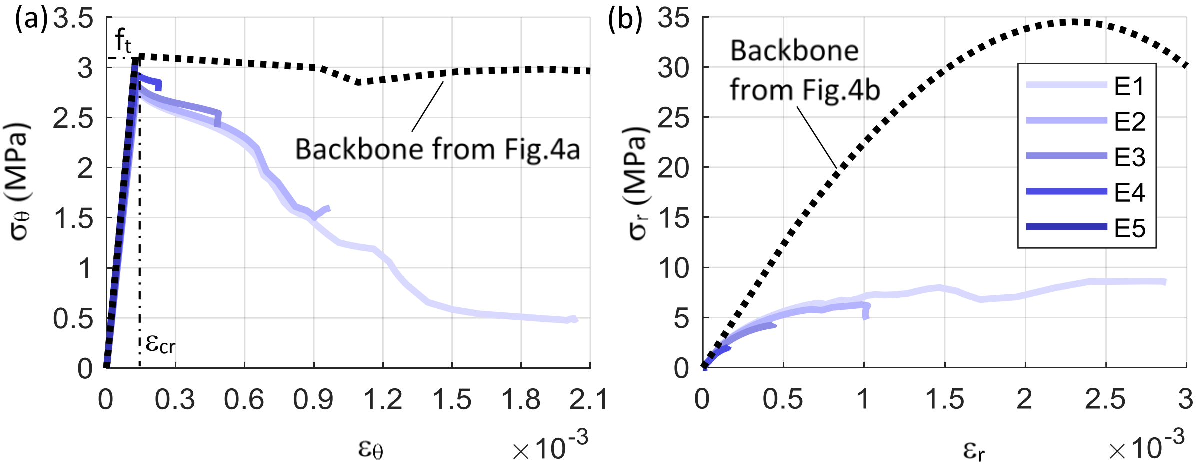

Fig. 8 Stress-strain responses for the five representing elements: (a) σ_θ vs. ε_θ; (b) σ_r vs. ε_r

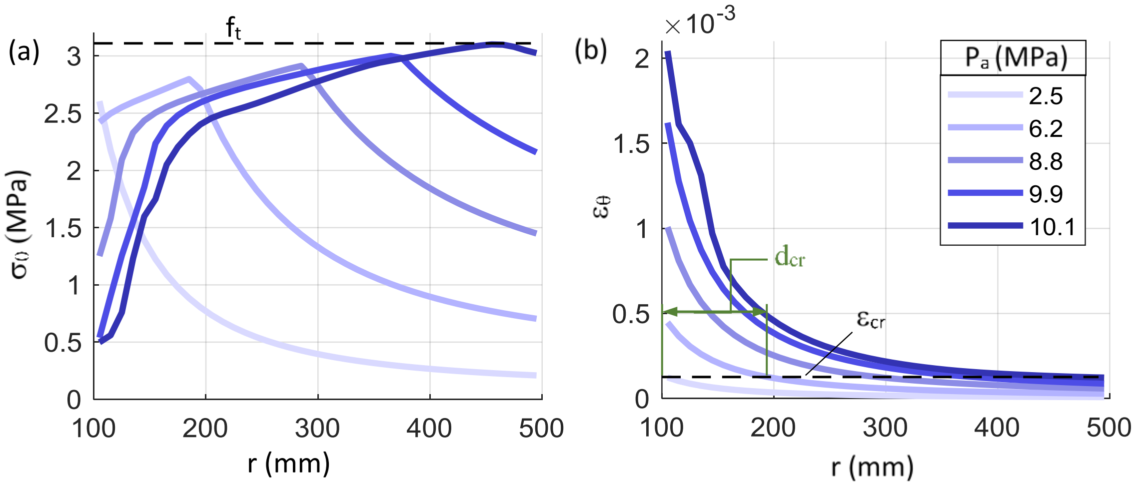

Fig. 9 Circumferential response distribution along the radius direction: (a) stress; (b) strain

significant crack penetration. This increasing penetration speed is probably because: as the crack penetrates through the section, the available elastic concrete section becomes thinner. As such, the pile section changes from a relatively thick-walled section to a relatively thin-walled section, where the thin-walled section has much higher but more uniform distributed circumferential stress than that of the thick-walled section as observed in Section 4.3 and Zhang *et al*. (2018). This relatively high and uniformly distributed stress demand makes the crack penetration faster. As also noticed in Fig. 10, the crack starts before the P_a reaches the f_t due to the strength reduction under the combined tension and compression response (Kupfer, BH. and Gerstle 1973).

Figure 11 shows the damage parameter (SDEG) for: (a) the five representing elements with the increase of P_a and (b) the distribution along the r direction at different P_a. As expected, the element (E1) closest to the inner surface exhibits largest damage response up to SDEG=0.72 as observed in Fig. 11a. As seen in Fig. 11b, the damage of the concrete mainly occurs within the first half of the section thickness (100 mm < r < 300 mm) because the crack penetration becomes fast as it closes to the outer surface and the concrete has no time to develop plastic responses.

4.2 Parametric results

This section discusses the effect of three parameters, including the inner diameter of the pile (d_i), the concrete grade, and the fiber content, on the response of the fiber reinforced concrete under the applied pressure (P_a). The results for different d_i are shown in this section with a fixed concrete grade of C30 and fiber content of 1.5%. The results shown for different concrete grades and fiber contents are shown in this section with a fixed d_i=200mm.

Figure 12 shows the circumferential stress (σ_θ) vs. applied pressure (P_a) for the element closest to the inner surface (E1) and the element closest to the outer surface (E5) with different inner diameters of the pile (d_i). As seen in Fig. 12, the P_a decreases as the increase of the d_i. Given the fact that the P_a was continuously increasing till the full cracking of the section, a much smaller pressure is expected to achieve the full section crack for a larger d_i. As the d_i increases (see Fig.12a), less strength degradation is observed in the element closest to the inner surface (E1). This behavior is because as the section becomes thinner, the element closest to the outer surface (E5) quickly reaches the cracking point (see Fig. 12b) and there is no enough time to

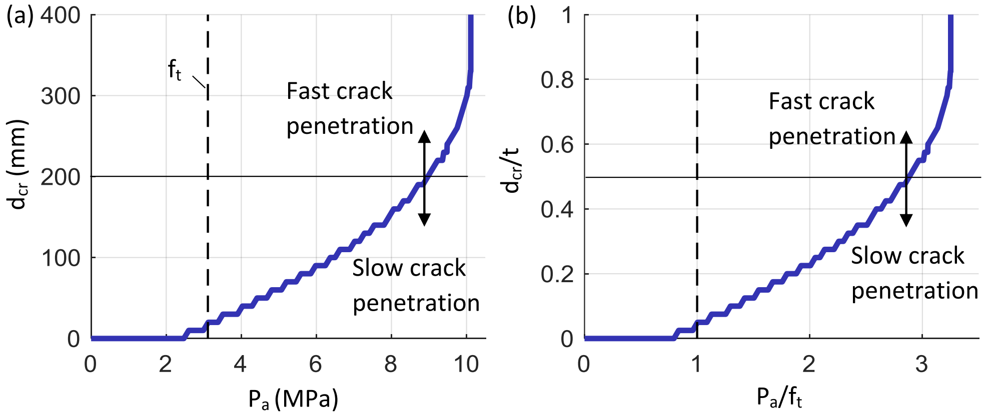

Fig. 10 Crack depth vs. applied pressure: (a) absolute values; (b) normalized values

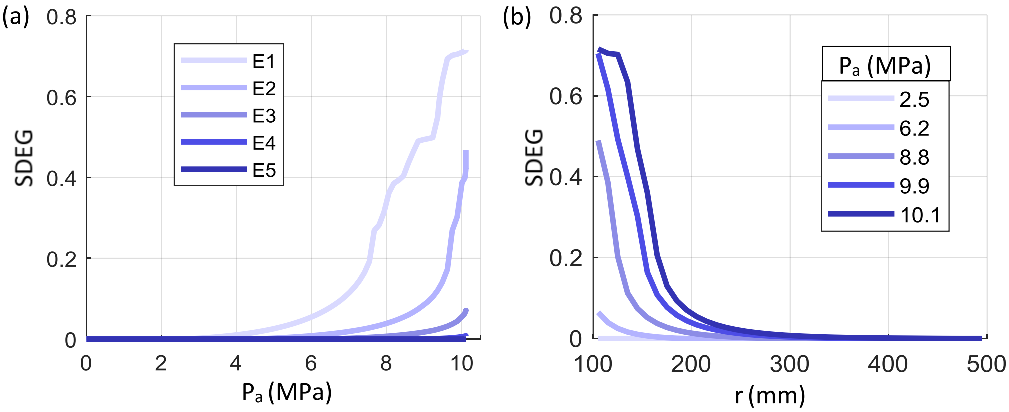

Fig. 11 Damage parameter vs.: (a) applied pressure; (b) radius

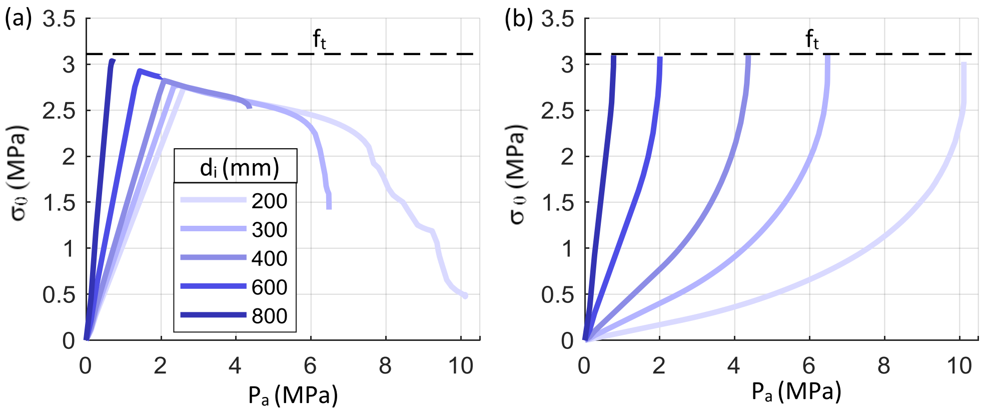

Fig. 12 Circumferential stress vs. applied pressure for different d_i for Element: (a) E1; (b) E5

develop post-cracking plastic responses inside the concrete section.

Figure 13 shows the circumferential stress (σ_θ) distribution along the r direction for the different d_i at two different states: (a) elastic when d_{cr}=0 and (b) post-cracking state when d_{cr}=t/2. As seen in Fig. 13a, the elastic stress distribution is non-uniform when d_i=200 mm. As d_i increases, a more uniform stress distribution is observed especially for the d_i=800 mm case. At plastic state as shown in Fig. 13b, the smaller d_i cases exhibit much more plastic stress redistribution than the cases of larger d_i.

Figure 14 shows the normalized crack depth (d_{cr}/t) vs. normalized pressure (P_a/f_t) and concrete damage parameter (SDEG) vs. P_a for different d_i cases. As seen in Fig. 14a, as the d_i increases, the crack penetration speed increases rapidly. Especially for the d_i=800mm case, the pressures for the initial and fully cracking are almost the same. This rapid crack penetration is due to the relatively uniform stress distribution for the thinner sections as shown in Fig. 13a, where the entire section reaches the cracking strain almost at the same time so that there is no time to develop the post-cracking plastic response. Thus, in turn, less concrete damage is observed in the cases of larger inner diameters as shown in Fig. 14b.

Figure 15 shows the circumferential stress (σ_θ) of the element closest to the inner surface (E1) for different

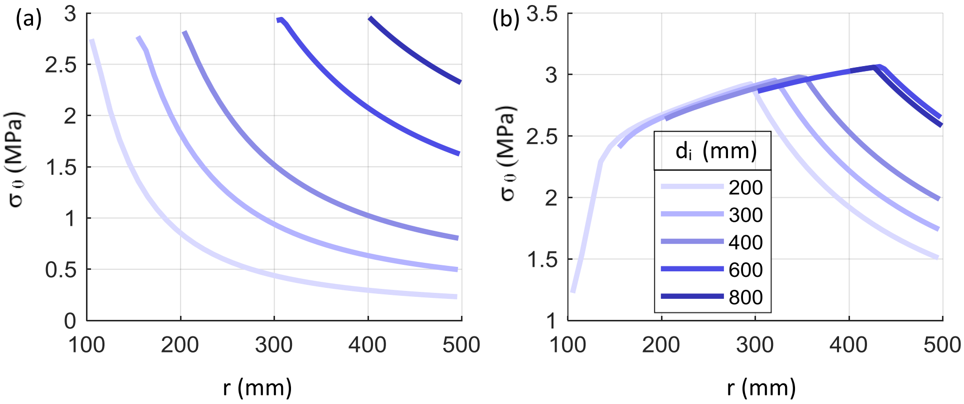

Fig. 13 Circumferential stress vs. r for different d_i at: (a) elastic state; (b) post-cracking state

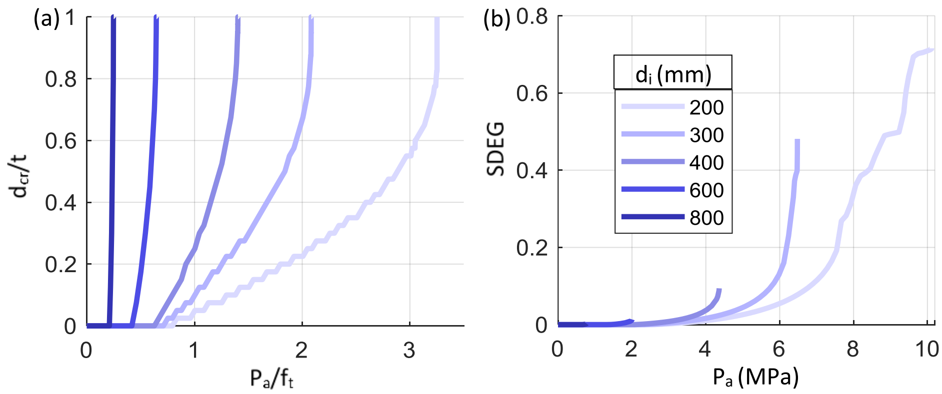

Fig. 14 Applied pressure for different d_i vs.: (a) normalized d_{cr}; (b) SDEG

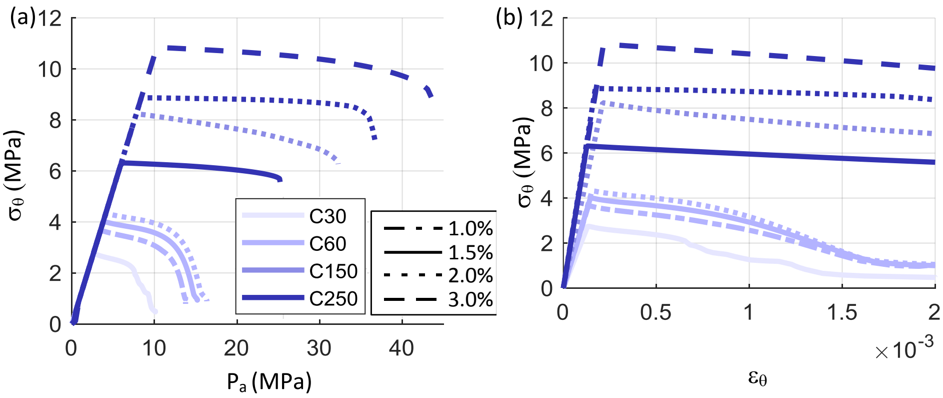

Fig. 15 Circumferential stress of E1 for different concrete grades and fiber contents vs. (a) applied pressure; (b) circumferential strain

concrete grades and fiber contents. As seen Fig. 15a, in general as the concrete grade and fiber content increase, the applied pressure (P_a) increases. This trend means that the required pressure for fully penetrating the entire section increases with the increase of the concrete grade and the fiber content. This behavior is consistent with the fact that as the concrete grade and the fiber content increase, the tensile strength (f_t) increases (refer to Fig.4a). The effect of the concrete grade is larger than that of the fiber content. As seen in Fig. 15b, higher concrete grade and fiber content have a less plastic strength degradation after cracking because a more ductile post-crack response is expected (refer to Fig. 4a). For C250 grade concrete, slight strain-softening behavior is seen in Fig. 15b rather than the hardening behavior observed in Fig.4a. This softening behavior is probably due to the combined tension and compression effect.

Figure 16 shows the crack depth (d_{cr}) and the damage parameter (SDEG) of E1 vs. the applied pressure (P_a) for different concrete grades and fiber contents. As seen in Fig. 16a, the crack penetration is faster for the lower grade concrete (C30 and C60) but much slower for higher grade concrete (C150 and C250). Thus, higher applied pressure is expected in the higher grade concrete at a given crack depth. As seen in Fig. 16b, larger plastic damage is observed in the lower grade concrete, which is consistent with the results shown in Fig. 15b.

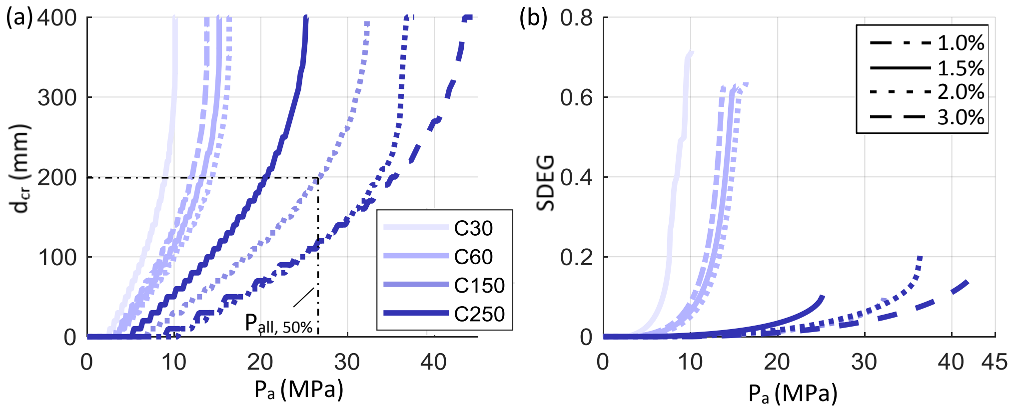

Fig. 16 Applied pressure for different concrete grades and fiber contents vs.: (a) d_{cr}; (b) SDEG

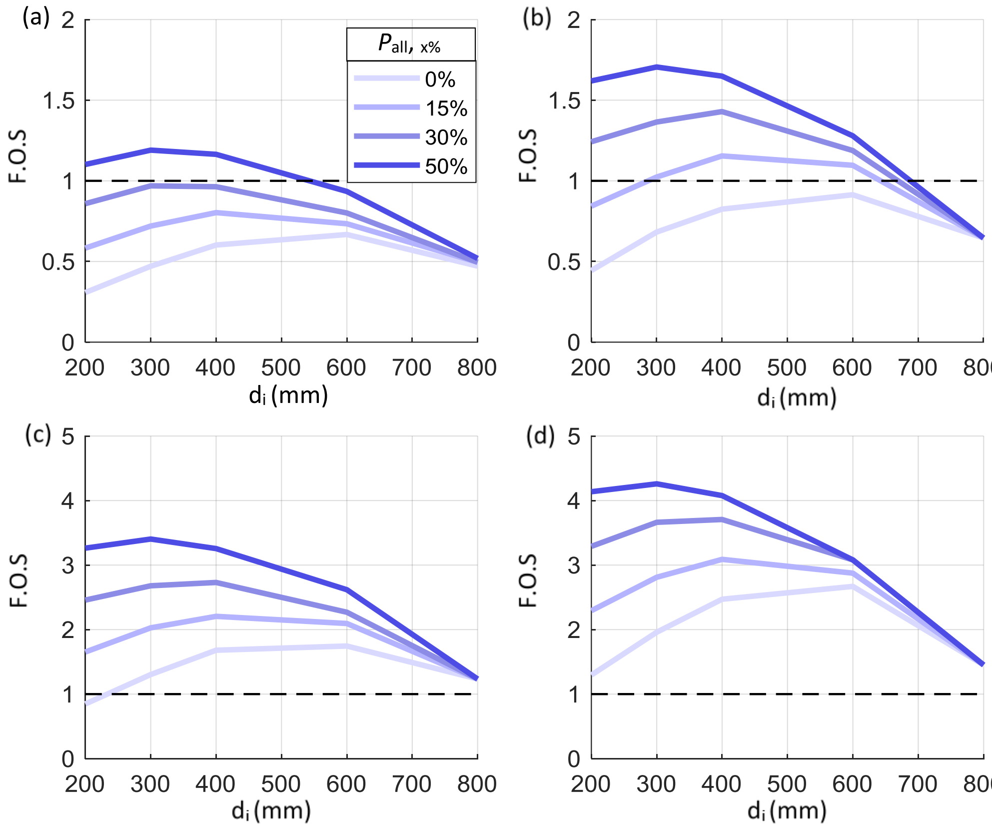

Fig. 17 Factor of safety at different crack penetration levels: (a) C30; (b) C60; (c) C150; (d) C250

4.3 Design recommedations

To quantify the capacity of the fiber reinforced concrete pile section at a given crack width for different cases considered in this paper, a new variable ($P_{\mathrm{all},\ x\%}$) can be defined as the allowable pressure at x% of crack penetration level, where x can be calculated as $100d_{cr}/t$. The procedure to determine this new variable is illustrated in Fig.16a. As an example of determining $P_{\mathrm{all},50\%}$ for C150 concrete, 2% fiber content and d_i=200mm, a horizontal trend line was first drawn at d_{cr}=200mm (x=$100d_{cr}/t$=50). The intersection between this horizontal trend line and the C150, 2% fiber content curve was then identified. A vertical trend line was plotted from the intersection to the X-axis to determine the value of $P_{\mathrm{all},50\%}$ as 26.5 MPa.

The allowable pressure at different crack penetration levels were compared to the pressure demand (P_D) in Fig. 3 of Section 2.3 by introducing a factor of safety (F.O.S). Only maximum pressure demand among the different column spaces and number of stories was considered since the variation over these two parameters is not significant (Refer to Fig.3). The factor of safety can then be calculated as $P_{\mathrm{all},\ x\%}$ / $P_{D,\max}$, where $P_{D,\max}$ is maximum pressure demand for different inner diameters of the pile section. Figure 17 shows the F.O.S vs. d_i at different crack penetration levels for (a) C30 with 1.5% fiber content; (b) C60 with 1.5% fiber content; (c) C150 with 2% fiber content; and (d) C250 with 2% fiber content. The crack

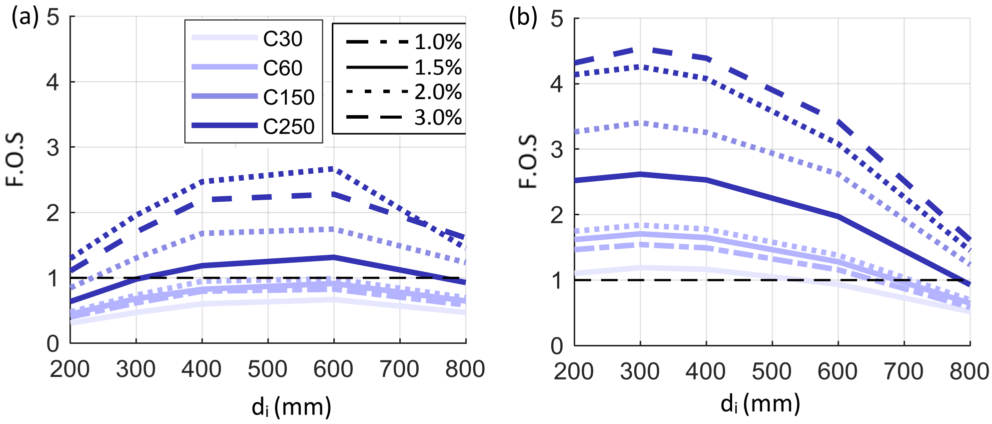

Fig. 18 Design charts for the energy storage pile foundation: (a) elastic design; (b) inelastic design

penetration level presented in Fig. 17 is limited as 50% since crack will quickly penetrate through the entire section afterwards which is not suitable as design targets as discussed in Section 4.1.

As seen in Fig. 17, the F.O.S at a given crack penetration level increases with the increase of the concrete grade. For the ultra high performance concrete (C150 and C250), it is even possible to have a crack free design (elastic design) when the F.O.S of $P_{\mathrm{all},\ 0\%}$ is large than 1.0.

As seen in Fig. 17, for small inner diameter cases (thick-walled section), the F.O.S increases significantly as the increase of the crack penetration level. However, for large inner diameter cases (thin-walled section), the F.O.S nearly remains unchanged as the increase of the crack penetration level. Thus, an inelastic design option, where partial cracking is allowed, is more suitable for the small inner diameter cases. The large inner diameter (d_i>600 mm) is not recommended for the inelastic design option.

Figure 18 presents two design charts to identify the factor of safety for the energy storage pile foundation with the fiber reinforced concrete. The 1st one shown in Fig.18a is for the elastic design (crack free design), where the F.O.S is corresponding to the $P_{\mathrm{all},\ 0\%}$. The 2nd chart shown in Fig.18b is for the inelastic design (crack is allowed but up to 50% of crack penetration level), where the F.O.S is corresponding to the $P_{\mathrm{all},\ 50\%}$. In generally, higher grade of concrete and fiber content can provide larger F.O.S for both elastic and inelastic design. For the elastic design, the inner diameter ranged from 400 mm to 600 mm can provide higher F.O.S. For the inelastic design, the small inner diameter (d_i<400 mm) can generally provide higher F.O.S.

5. Conclusions

This paper investigates the nonlinear structural response of the fiber reinforced concrete pile foundation subjected to pressure from the compressed air. The nonlinear finite element simulations were conducted using 2D plane strain model with the concrete damage plasticity. The following conclusions can be drawn for the general structural response with the increase of the applied pressure till the full cracking of the entire pile section:

(1) As applied pressure increases, the pile section gradually reaches the cracking point and exhibits post-cracking strength degradation behavior in a sequence from the inner surface to the outer surface.

(2) The uniaxial strength of the concrete cannot be reached due to the combined tension (in the circumferential direction) and compression (in the radius direction) stresses. This strength reduction is more significant for compression since the pile section was loaded against its tension limit. The combined stresses result in more rapid strength degradation after cracking comparing to the uniaxial tension.

(4) The circumferential stress is redistributed after the concrete gradually enters the post-cracking response from the inner to outer surface. When the entire section reaches the cracking point, the stress distribution is directly opposite to the one in the elastic response.

(5) The crack penetrates from the inner to outer surface as the increase of the applied pressure. The penetration speed is initially slow but increases due to the reduction of available elastic section. The penetration speed increases significantly when the crack develops more than 50% of the section thickness,

(6) The concrete near the inner surface exhibits severer plastic damages than that near the outer surface, where the post-cracking plastic response has no time to be developed due to the fast crack penetration.

Several parameters were considered in the study including the concrete grade, the fiber content and the inner diameter of the pile. The following conclusions can be drawn for the effects of these parameters on the structural response of the fiber reinforced concrete pile:

(1) As the inner diameter increases: the pile section resists less applied pressure before the crack fully penetrates the entire section; the circumferential stress redistribution becomes insignificant; the crack penetration speed significantly increases since large inner diameter results in a more uniform stress distribution along the radius direction, where the entire pile section can reach the cracking point nearly at the same time; less plastic damages are observed in the concrete section due to the faster crack penetration.

(2) As the concrete grade and the fiber content increase: the pile section can resist more applied pressure before the

crack fully penetrates the entire section; the crack penetration speed decreases, which results in a higher allowable applied pressure at a given crack depth; less plastic damage is observed due to a more ductile post-cracking behavior.

The allowable pressure at a given crack penetration level was calculated and compared to the pressure demand for typical buildings. Elastic and inelastic design charts to identify the factor of safety were developed in Fig.18 for all the concrete grades, the fiber contents, and the inner diameters of the pile section studied in this paper. The following design recommendations can be made:

(1) The inelastic design target is recommended to be set as crack penetration level less than 50% to avoid possible full section cracking and air leakage.

(2) The large inner diameter (d_i>600 mm) of the pile section is not recommended.

(3) The inner diameter ranged from 400mm to 600mm is recommended for the elastic (crack free) option for the ultra-high-performance concrete (C150 or C250).

(4) The small inner diameter (d_i<400 mm) is recommended for the inelastic design option, which can be used in both high grade and low concrete grade (e.g. C60) concrete.

Acknowledgments

This research was supported by the Nazarbayev University Research Fund under Grant (#SOE2017001) "Development of a Renewable Energy Storage System using Reinforced Concrete Foundations". The authors are grateful for this support. Any opinions, findings, and conclusions or recommendations expressed in this material are those of the author(s) and do not necessarily reflect the views of the Nazarbayev University.

References

ABAQUS (2010), "Abaqus 6.10 analysis user's manual", Dassault Systèmes; France.

Agibayeva, A., Ju, H., Zhang, D., Moon, S.W., Kim, J. and Lee, D.H. (2018), "Application of CFT Pile foundation as an energy storage media, joint NU-SNU mini-symposium on the design and analysis of innovative structural and geotechnical systems", *The 2018 International Conference on Advances in Computational Design*, Incheon, Korea, August.

Bektimirova, U., Shon, C., Zhang, D., Sharafutdinov, E. and Kim, J. (2018), "Proportioning and characterization of reactive powder concrete for an energy storage pile application", *Appl. Sci.,* **8**(12), 2507. https://doi.org/10.3390/app8122507.

Bektimirova, U., Tleuken, A., Satekenova, E., Shon, C., Zhang, D. and Kim, J. (2017), "Preliminary experimental investigation on the strength and air permeability of reactive powder concrete", *Mater. Sci. Forum,* **917**, 321-328. https://doi.org/10.4028/www.scientific.net/MSF.917.321.

Drucker, D.C. and Prager, W. (1952), "Soil mechanics and plastic analysis on limit design", *J. Appl. Math.,* **10**, 157-165.

Fédération internationale du béton (2008), *Constitutive Modelling of High Strength/high Performance Concrete*, The International Federation for Structural Concrete (*fib*), Switzerland.

Hafezolghorani, M., Hejazi, F., Vaghei, R., Jaafar, M.S.B. and Karimzade, K. (2017), "Simplified damage plasticity model for concrete", *Struct. Eng. Int.,* **27**(1), 68-78.

Hassan, A.M.T., Jones, S.W. and Mahmud, G.H. (2012), "Experimental test methods to determine the uniaxial tensile and compressive behavior of ultra high performance fiber reinforced concrete (UHPFRC)", *Construct. Build. Mater.* **37**, 874-882. https://doi.org/10.1016/j.conbuildmat.2012.04.030.

Hayter, S. and Kandt, A. (2011), "Renewable energy applications for existing buildings", NREL/CP-7A40-52172; National Renewable Energy Lab. (NREL), Golden, CO, USA.

Kim, S., Ko, J., Kim, S., Soo, H. and Tummalapudi, M. (2017), "Investigation of a small-scale compressed air energy storage pile as a foundation system", *Geotechnical Frontiers 2017,* Orlando, Florida, USA, March. https://doi.org/10.1061/9780784480472.011.

Ko, J., Seo, H., Kim, S. and Kim, S. (2018), "Numerical analysis for mechanical behavior of pipe pile utilized for compressed air energy storage", *IFCEE 2018*, Orlando, Florida, USA, March. https://doi.org/10.1061/9780784481578.068.

Kupfer, B.H. and Gerstle, K.H. (1973), "Behavior of concrete under biaxial stresses", *J. Eng. Mech. Division*, **99**(4), 853-866.

Kwak, Y.K., Marc, O.E., Kim, W.S. and Kim, J. (2002), "Shear strength of steel fiber-reinforced concrete beams without stirrups", *ACI Struct. J.,* **99**(4), 530-538. https://doi.org/10.4025/actascitechnol.v36i3.19005.

Kwan, A.K.H. and Chu, S.H. (2018), "Direct tension behavior of steel fiber reinforced concrete measured by a new test method", *Eng. Struct.,* **176**(2018), 324-336. https://doi.org/10.1016/j.engstruct.2018.09.010.

Lee, S.C., Oh, J.H. and Cho, J.Y. (2016), "Fiber efficiency in SFRC members subjected to uniaxial tension", *Construct. Build. Mater.,* **113**(2016), 479-487. https://doi.org/10.1016/j.conbuildmat.2016.03.076.

Rugolo, J. and Aziz, M. (2012), "Electricity storage for intermittent renewable sources", *Energy Environ. Sci.,* **5**(5), 7151-7160.

Sabirova, A., Zhang, D., Kim, J., Nguyen, M. and Shon, C. (2016), "Development of a reinforced concrete foundation system for renewable energy storage", *Proceedings of the 8th Asian Young Geotechnical Engineering Conference,* Astana, Kazakhstan, August.

Sun, M., Chen, Y., Zhu, J., Sun, T., Shui, Z., Ling, G., Zhong, H. and Zheng, Y. (2019), "Effect of modified polyvinyl alcohol fibers on the mechanical behavior of engineered cementitious composites", *Materials,* **12**(1), 37. https://doi.org/10.3390/ma12010037.

Tulebekova, S., Saliyev, D., Zhang, D., Kim, J., Karabay, A., Turlybek, A. and Kazybayeva, L. (2017), "Preliminary analytical study on the feasibility of using reinforced concrete pile foundations for renewable energy storage by compressed air energy storage technology", *IOP Conference Series: Materials Science and Engineering,* IOP Publishing Ltd., London, United Kingdom.

Wan, G., Fleischman, R.B. and Zhang, D. (2012), "Effect of spandrel beam to double tee connection characteristic on flexure-controlled precast diaphragms", *ASCE J. Struct. Eng.*, **138**(2), 247-258. https://doi.org/10.1061/(ASCE)ST.1943-541X.0000426.

Wan, G., Zhang, D., Fleischman, R.B. and Naito, C.J. (2015), "A coupled connector element for nonlinear static pushover analysis of precast concrete diaphragms", *Eng. Struct.*, **86**(1), 58-71. https://doi.org/10.1016/j.engstruct.2014.12.029.

Walahathantri, B.L., Thambiratnam, D.P., Chan, T.H.T. and Fawzia, S. (2011), "A material model for flexural crack simulation in reinforced concrete elements using ABAQUS", *eddBE2011 Proceedings*.

Wille, K., El-Tawil, S. and Naaman, A.E. (2014), "Properties of strain hardening ultra high performance fiber reinforced concrete

(UHP-FRC) under direct tensile loading", *Cement Concrete Compos.,* **48**(2014), 53-66. https://doi.org/10.1016/j.cemconcomp.2013.12.015.
Yoo, D.Y. and Banthia, N. (2015), "Numerical simulation on structural behavior of UHPFRC beams with steel and GFRP bars", *Comput. Concrete*, **5**, 759-774. https://doi.org/10.12989/cac.2015.16.5.759.
Yu, K., Jiangtao, Y., Dai, J.G., Lu, Z.D. and Shah, S.P. (2017), "Development of ultra-high performance engineered cementitious composites using polyethylene (PE) fibers", *Construct. Build. Mater.,* **158**, https://doi.org/10.1016/j.conbuildmat.2017.10.040.
Zhang, D., Fleischman, R.B., Naito, C.J. and Zhang, Z. (2016). "Development of diaphragm connector elements for three-dimensional nonlinear dynamic analysis of precast concrete structures", *Adv. Struct. Eng.*, **19**(2), 187-202. https://doi.org/10.1177/1369433215624319.
Zhang, D., Kim, J., Tulebekova, S., Saliyev, D. and Lee, D.H. (2018), "Structural responses of reinforced concrete pile foundations subjected to pressures from compressed air for renewable energy storage", *J. Concrete Struct. Mater.,* **12**, 74. https://doi.org/10.1186/s40069-018-0294-z.
Zhang, L., Ahmari, S., Sternberg, B. and Budhu, M. (2012), "Feasibility study of compressed air energy storage using steel pipe piles", *GeoCongress 2012*, California, USA, March. https://doi.org/10.1061/9780784412121.439.
Zhu, H., Wan, K.T., Satekenova E., Zhang, D., Leung C. and Kim J. (2018) "Development of lightweight strain hardening cementitious composite for structural retrofit and energy efficiency improvement of unreinforced masonry housings", *Construct. Build. Mater.*, **167**, 791-812. https://doi.org/10.1016/j.conbuildmat.2018.02.033.

CC

Notations

C = adiabatic constant;

d_{cr} = crack depth on the pile section;

d_i = inner diameter of the pile section;

d_o = outer diameter of the pile section;

E = Young's modulus of the concrete;

f_{b0}/f_{c0} = ratio of biaxial compressive to uniaxial compressive strength;

$f_{c,,t}$ = concrete compression, tension strength;

K = ratio of the 2nd stress invariant on the tensile meridian to that on the compressive meridian;

P_a = applied inner air pressure;

$P_{all,x\%}$ = allowable pressure at x% of crack penetration;

P_D = pressure demand from thermodynamic cycles;

$P_{D,max}$ = maximum pressure demand for different inner diameters of the pile section;

R = universal gas constant;

r = radius direction of the pile section;

r_i = inner radius of the pile section;

r_0 = outer radius of the pile section;

SDEG = damage parameter from concrete damage plasticity model;

T_1 = ambient air temperature;

t = thickness of the pile section;

t_{in} = time for compressing air;

V_s = available volume for storage;

$\dot{w}_{in}$ = available energy for storage;

ε = eccentricity;

ε_{cr} = cracking strain;

ε_r = radial strain in the pile section;

ε_θ = circumferential strain in the pile section;

φ = dilation angle (in degrees);

η_1 = efficiency for compressing air;

μ_v = viscosity parameter;

μ = molar mass of the air;

θ = circumferential direction;

ρ_1 = initial density of the air;

σ_θ = circumferential stress in the pile section;

σ_r = radial stress in the pile section;

σ_v = vertical stress in the pile section.